

# Chromism of Bi<sub>2</sub>WO<sub>6</sub> in single crystal and nanosheet forms†

Cite this: DOI: 10.1039/c3tc32070g

Timothy R. Pope, Melissa N. Lassig, Gregory Neher, Richard D. Weimar III and Tina T. Salguero\*

Nanosheets of Bi<sub>2</sub>WO<sub>6</sub> with lateral dimensions of 1–2 μm and thicknesses of 5–15 nm were prepared using Cs<sub>4</sub>W<sub>11</sub>O<sub>36</sub><sup>2-</sup> nanosheets as the tungsten oxide precursor and lateral template. The formation of these nanosheets was followed by electron microscopy and powder X-ray diffraction techniques. The isolated Bi<sub>2</sub>WO<sub>6</sub> nanosheet product was characterized with respect to structure, morphology, spectroscopic properties, and optical properties. The bandgap energy of Bi<sub>2</sub>WO<sub>6</sub> nanosheets is relatively large at ~3.1 eV. The chromism of these sheets with respect to UV irradiation and Li<sup>+</sup> intercalation was examined in detail. The UV-induced photochromism of dispersed Bi<sub>2</sub>WO<sub>6</sub> nanosheets is highly dependent on the solvent environment, and the initial color change from white to black is reversible. The photochromic properties of “flowerlike” and single crystal Bi<sub>2</sub>WO<sub>6</sub> were evaluated as well. Another color change, pale yellow to brown-black, occurred when lithium ions were intercalated into the Bi<sub>2</sub>WO<sub>6</sub> lattice using *n*-butyl lithium. Reaction of lithiated Bi<sub>2</sub>WO<sub>6</sub> with water yielded nanofragments of Bi<sub>2</sub>WO<sub>6</sub> rather than nanosheets.

Received 18th October 2013  
Accepted 15th November 2013

DOI: 10.1039/c3tc32070g

www.rsc.org/MaterialsC

## Introduction

Bismuth tungstate (Bi<sub>2</sub>WO<sub>6</sub>) is a textbook example of the Aurivillius family of layered perovskite-like metal oxides. Its structure consists of alternating layers of Bi<sub>2</sub>O<sub>2</sub> and corner sharing WO<sub>6</sub> octahedra (Fig. 1E).<sup>1</sup> Bi<sub>2</sub>WO<sub>6</sub> is a stable high-temperature ferroelectric material with a Curie temperature of 940 °C, and it displays a larger spontaneous polarization than other bismuth layer-based ferroelectrics.<sup>2,3</sup> This material also has a high electromechanical coupling coefficient, making it suitable for high-temperature piezoelectric applications.

Most recent studies of Bi<sub>2</sub>WO<sub>6</sub> have focused on its activity for photocatalysis, especially applied to the destruction of organic molecules.<sup>4,5</sup> It has high photogenerated hole mobility and catalytic performance because the bismuth 6s orbitals hybridize with the oxygen 2p orbitals to create a hybridized valence band.<sup>6</sup>

Bi<sub>2</sub>WO<sub>6</sub> is formed readily by the solid state reaction of Bi<sub>2</sub>O<sub>3</sub> and WO<sub>3</sub>, and mm-sized single crystals can be grown from melt fluxes containing Li<sub>2</sub>B<sub>4</sub>O<sub>7</sub>.<sup>6,7</sup> Furthermore, there are many examples of micro- and nanostructured Bi<sub>2</sub>WO<sub>6</sub> produced under hydrothermal conditions,<sup>4,5</sup> which has become a preferred method to control photocatalytic performance *via* particle size, morphology, surface area, and chemical surface

functionality. In a typical hydrothermal synthesis, a precursor mix of Na<sub>2</sub>WO<sub>4</sub> and Bi(NO<sub>3</sub>)<sub>3</sub> react to form stacked layers of Bi<sub>2</sub>WO<sub>6</sub> nanosheets.<sup>4</sup> Layers preferentially undergo anisotropic growth, expanding laterally instead of vertically. Typical products include micron-sized “flowerlike” clusters of Bi<sub>2</sub>WO<sub>6</sub> platelets,<sup>8,9</sup> although morphologies can be influenced by pH or the use of a surfactant.<sup>10–20</sup>

A cation-deficient analog of the Aurivillius phase is Bi<sub>2</sub>W<sub>2</sub>O<sub>9</sub>.<sup>21</sup> In pioneering studies, Schaak and Mallouk showed that acid leaching bismuth oxide from Bi<sub>2</sub>W<sub>2</sub>O<sub>9</sub> provides a colloidal dispersion of H<sub>2</sub>W<sub>2</sub>O<sub>7</sub> nanosheets, a layered-perovskite solid acid.<sup>22</sup> Subsequent studies by Osterloh and co-workers showed that sub-nm thick nanosheets of WO<sub>3</sub> (formally H<sub>2</sub>W<sub>2</sub>O<sub>7</sub> stabilized with tetrabutylammonium cations) have photocatalytic hydrolysis properties comparable to bulk WO<sub>3</sub>.<sup>23</sup>

When exposed to UV light, nanosized WO<sub>3</sub> undergoes a photochromic shift in which the once clear material darkens significantly.<sup>24–26</sup> Thus, WO<sub>3</sub> and metal-doped derivatives have been investigated as candidates for electrochromic devices, specifically “smart windows” that regulate the transmission of sunlight.<sup>27–29</sup> Inorganic electrochromic devices are favorable because they display high UV-stability, a wide operational temperature range, high contrast, viewing angle independence, and variable coloration intensities.<sup>30</sup>

Various other tungsten oxide derivatives also exhibit photochromic properties. For instance, Sasaki and co-workers have reported tungstate-based nanosheets derived from layered Cs<sub>6+x</sub>W<sub>11</sub>O<sub>36</sub> and Rb<sub>4</sub>W<sub>11</sub>O<sub>35</sub> materials that darken under UV irradiation.<sup>26,31</sup>

Department of Chemistry, The University of Georgia, Athens, GA 30602, USA. E-mail: salguero@uga.edu; Tel: +1 706-542-6376

† Electronic supplementary information (ESI) available: Synthesis and additional characterization of Cs<sub>4</sub>W<sub>11</sub>O<sub>36</sub><sup>2-</sup> nanosheets, additional characterization of Bi<sub>2</sub>WO<sub>6</sub> nanosheets, and preparation of Bi<sub>2</sub>WO<sub>6</sub> single crystals. See DOI: 10.1039/c3tc32070g

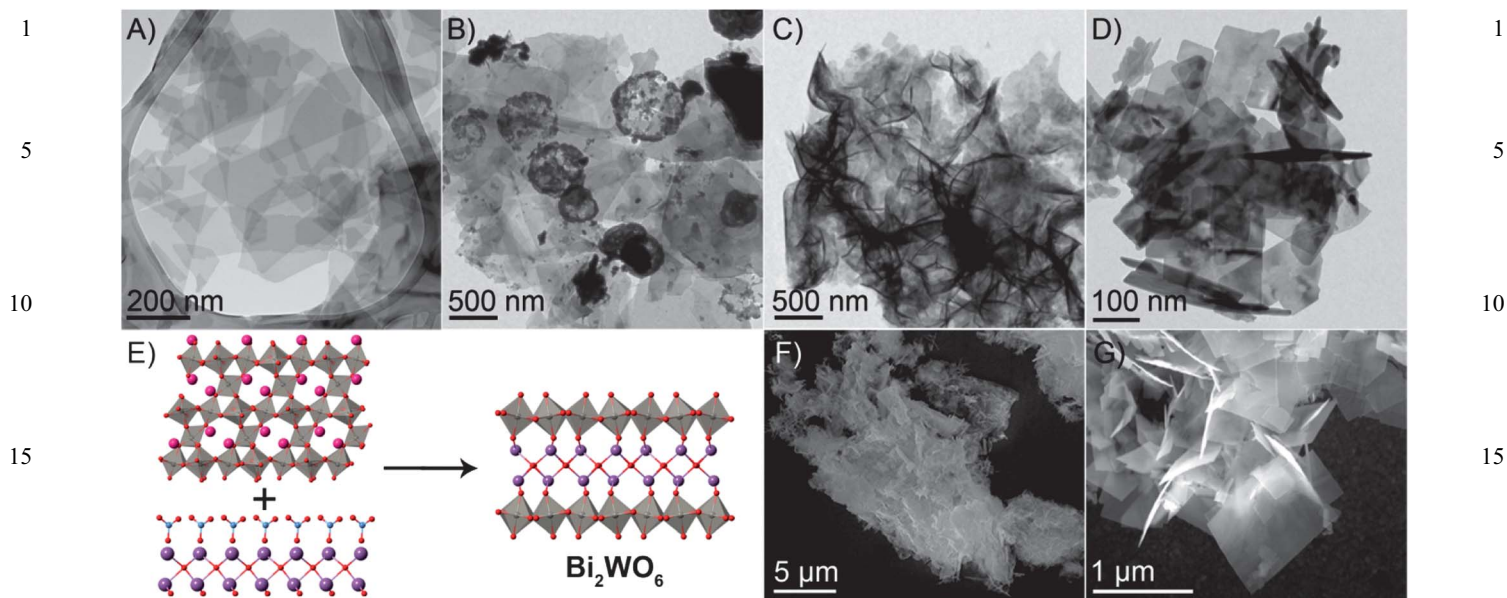


Fig. 1 (A) TEM image of the  $\text{Cs}_4\text{W}_{11}\text{O}_{36}^{2-}$  nanosheet precursor. (B) TEM image of  $\text{Cs}_4\text{W}_{11}\text{O}_{36}^{2-} + \text{Bi}(\text{NO}_3)_3$  reaction mixture at 0.5 h. (C and F) TEM and SEM images, respectively, of the reaction mixture at 2 h. (D and G) TEM and SEM images, respectively, of the reaction mixture at 5 h. (E) Reaction scheme illustrating the transformation of a tungsten oxide nanosheet precursor (side view along the  $b$ -axis)<sup>32</sup> and a bismuth oxide hydroxide nitrate (side view along the  $a$ -axis)<sup>33</sup> into  $\text{Bi}_2\text{WO}_6$  nanosheets (side view along the  $c$ -axis).<sup>34</sup>

In this contribution, we discuss the chromism of  $\text{Bi}_2\text{WO}_6$  with several examples. We find that the photochromism of dispersed  $\text{Bi}_2\text{WO}_6$  nanosheets is highly dependent on solvent choice, and that the color change is reversible. Additionally, we compare the photochromism of  $\text{Bi}_2\text{WO}_6$  nanosheets with that of  $\text{Bi}_2\text{WO}_6$  in flowerlike clusters and single crystal form. In another case, we find that chromism also can be induced by the intercalation of lithium ions into the  $\text{Bi}_2\text{WO}_6$  structure.

## Results and discussion

### $\text{Bi}_2\text{WO}_6$ nanosheets from $\text{Cs}_4\text{W}_{11}\text{O}_{36}^{2-}$ nanosheets

The strategy we apply here uses  $\text{Cs}_4\text{W}_{11}\text{O}_{36}^{2-}$  nanosheets as the tungsten-containing precursor for  $\text{Bi}_2\text{WO}_6$  formation, together with a commonly used source of bismuth,  $\text{Bi}(\text{NO}_3)_3$ , and without the use of a pH buffer or surfactant. The  $\text{Cs}_4\text{W}_{11}\text{O}_{36}^{2-}$  nanosheets aid the formation of well-defined  $\text{Bi}_2\text{WO}_6$  nanosheets by acting as a template for nanosheet growth.

$\text{Cs}_4\text{W}_{11}\text{O}_{36}^{2-}$  nanosheets were prepared from  $\text{Cs}_{6+x}\text{W}_{11}\text{O}_{36}$  as described previously,<sup>26</sup> except without the addition of tetrabutyl ammonium (TBA) ligands. In this synthesis, silver-gray  $\text{Cs}_{6+x}\text{W}_{11}\text{O}_{36}$  crystals are fully exfoliated to yield a pearlescent white dispersion of  $\text{Cs}_4\text{W}_{11}\text{O}_{36}^{2-}$  nanosheets (Fig. S1†). Transmission electron microscopy (TEM) confirms the morphology of this product (Fig. 1A), and atomic force microscopy (AFM) shows that these nanosheets have an average thickness of 2.5 nm (Fig. S2†), which is comparable to the value of 2 nm reported for TBA-stabilized  $\text{Cs}_4\text{W}_{11}\text{O}_{36}^{2-}$  nanosheets.<sup>26</sup>

Occasionally the  $\text{Cs}_4\text{W}_{11}\text{O}_{36}^{2-}$  dispersion became yellow during the exfoliation process (Fig. S4†). Both TEM and powder X-ray diffraction (PXRD) analysis indicate that these samples contain restacked  $\text{Cs}_4\text{W}_{11}\text{O}_{36}^{2-}$  nanosheets. TEM images show

noticeably thicker, irregular multilayer structures (Fig. S5†). Increased ordering of the crystal structure, corresponding to thicker material, is corroborated by more intense PXRD patterns (Fig. S6†). Such restacked nanosheets do not display the same reactivity as the monolayer material and yield non-uniform  $\text{Bi}_2\text{WO}_6$  nanosheets, along with larger platelet and rod morphologies. Thus, in this work, only fully exfoliated  $\text{Cs}_4\text{W}_{11}\text{O}_{36}^{2-}$  was used to prepare  $\text{Bi}_2\text{WO}_6$  nanosheets. If restacking occurs, this material can be re-exfoliated with mild sonication in 12 M HCl.

Under hydrothermal conditions,  $\text{Cs}_4\text{W}_{11}\text{O}_{36}^{2-}$  nanosheets react with  $\text{Bi}(\text{NO}_3)_3$  over the course of several hours to form  $\text{Bi}_2\text{WO}_6$  nanosheets. Before discussing the characterization of this product, we describe a time study that provides some insight into the  $\text{Cs}_4\text{W}_{11}\text{O}_{36}^{2-}$  to  $\text{Bi}_2\text{WO}_6$  transformation. Electron microscopy images and PXRD data that correspond to several intermediate points along the reaction process are presented in Fig. 1 and 2.

After 0.5 h of reaction time, the initial  $\text{Bi}(\text{NO}_3)_3$  is transformed into  $[\text{Bi}_6\text{O}_5(\text{OH})_3](\text{NO}_3)_5 \cdot 3\text{H}_2\text{O}$ . The formation of distinctive circular bismuth oxide nanosheets/platelets is apparent by TEM (Fig. 1B), and this species is present in the PXRD pattern (Fig. 2). By the 1 h mark, however, all the  $[\text{Bi}_6\text{O}_5(\text{OH})_3](\text{NO}_3)_5 \cdot 3\text{H}_2\text{O}$  is converted into  $[\text{Bi}_6\text{O}_6(\text{OH})_3](\text{NO}_3)_3 \cdot 1.5\text{H}_2\text{O}$ . The PXRD pattern in Fig. 2 shows that initially highly crystalline  $[\text{Bi}_6\text{O}_6(\text{OH})_3](\text{NO}_3)_3 \cdot 1.5\text{H}_2\text{O}$  forms. Previous reports also have noted that  $\text{Bi}(\text{NO}_3)_3$  converts to  $[\text{Bi}_6\text{O}_6(\text{OH})_3](\text{NO}_3)_3 \cdot 1.5\text{H}_2\text{O}$  under similar hydrothermal conditions.<sup>35</sup> It appears that this species becomes the bismuth oxide source that reacts with  $\text{Cs}_4\text{W}_{11}\text{O}_{36}^{2-}$  nanosheets. In contrast, detailed *in situ* energy-dispersive X-ray diffraction experiments by Patzke and co-workers showed that only peaks

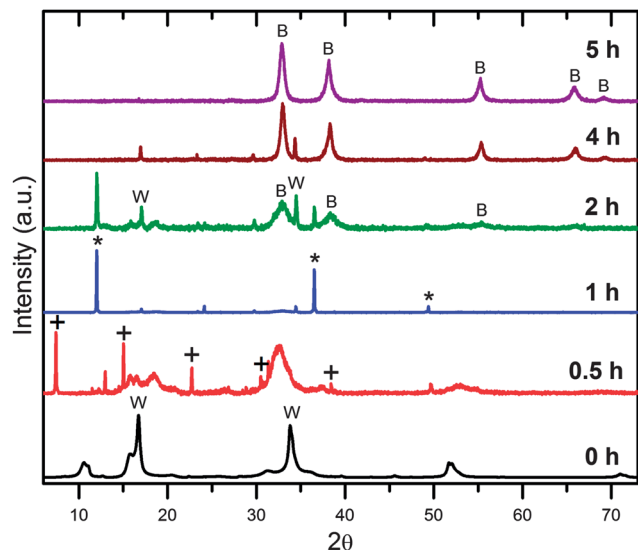


Fig. 2 PXRD patterns collected at intervals during the transformation of  $\text{Cs}_4\text{W}_{11}\text{O}_{36}^{2-}$  nanosheets into  $\text{Bi}_2\text{WO}_6$  nanosheets. Symbols for identified species include: + for  $[\text{Bi}_6\text{O}_5(\text{OH})_3](\text{NO}_3)_5 \cdot 3\text{H}_2\text{O}$  (JCPDS 00-053-1038), \* for  $[\text{Bi}_6\text{O}_6(\text{OH})_3](\text{NO}_3)_3 \cdot 1.5\text{H}_2\text{O}$  (JCPDS 00-048-0575), W for  $\text{Cs}_4\text{W}_{11}\text{O}_{36}^{2-}$ , B for  $\text{Bi}_2\text{WO}_6$  nanosheets.

corresponding to crystalline  $\text{Bi}_2\text{WO}_6$  are seen when  $\text{K}_2\text{WO}_4$  reacts with  $\text{Bi}(\text{NO}_3)_3$ .<sup>36</sup>

At the 2 h mark, formation of bismuth oxide from  $[\text{Bi}_6\text{O}_6(\text{OH})_3](\text{NO}_3)_3 \cdot 1.5\text{H}_2\text{O}$  is seen by TEM in Fig. 1C and by PXRD in Fig. 2. At this point the circular platelets become lateral sheets. As discussed by Zhang, *et al.*,  $\text{Bi}_2\text{WO}_6$  preferentially grows laterally along the *c*-axis.<sup>4</sup> In our present work, the morphology of the  $\text{Cs}_4\text{W}_{11}\text{O}_{36}^{2-}$  further promotes the formation of large two-dimensional crystals. However, the bismuth oxide is not yet fully incorporated, seen by the irregular clustering in the scanning electron microscopy (SEM) image (Fig. 1F) and the  $[\text{Bi}_6\text{O}_6(\text{OH})_3](\text{NO}_3)_3 \cdot 1.5\text{H}_2\text{O}$  peaks in the PXRD (Fig. 2). At this point in the reaction, we also observe a minor form of bismuth oxide with rod-like structure (see SEM image and EDS data in Fig. S7†). The concentration of  $[\text{Bi}_6\text{O}_6(\text{OH})_3](\text{NO}_3)_3 \cdot 1.5\text{H}_2\text{O}$  is markedly decreased by the 4 h mark as the reaction with  $\text{Cs}_4\text{W}_{11}\text{O}_{36}^{2-}$  progresses. PXRD confirms the corresponding increase in the concentration of  $\text{Bi}_2\text{WO}_6$  nanosheets (Fig. 2).

After 5 h at hydrothermal conditions, all of the cesium ions present in the  $\text{Cs}_4\text{W}_{11}\text{O}_{36}^{2-}$  crystal lattice have been leached out and the tungsten oxide reacts with bismuth oxide to form the  $\text{Bi}_2\text{WO}_6$  nanosheets. PXRD in Fig. 2 shows the clean formation of  $\text{Bi}_2\text{WO}_6$  and exhibits broad peak widths consistent with a nanostructured material. TEM and SEM images in Fig. 1D and G show that  $\text{Bi}_2\text{WO}_6$  forms nanosheet clusters but with no macrostructure, as opposed to the flowerlike morphologies obtained without the  $\text{Cs}_4\text{W}_{11}\text{O}_{36}^{2-}$  templates (Fig. S13†). Additionally, no bismuth oxide species are seen. The samples for this electron microscopy study were not ground prior to analysis, but when isolated  $\text{Bi}_2\text{WO}_6$  nanosheet products were prepared by grinding and mild sonication, we observed well-separated nanosheets. In particular, the SEM images in Fig. 3

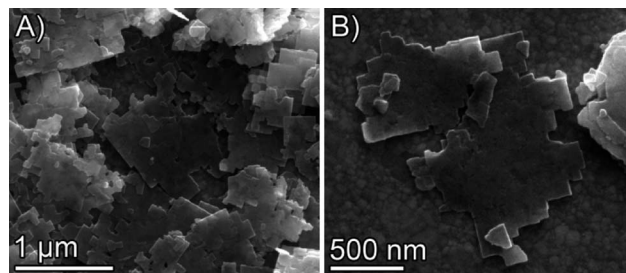


Fig. 3 SEM images of isolated  $\text{Bi}_2\text{WO}_6$  nanosheets that highlight the morphology of this material. Image (B) clearly shows that typical lateral dimensions are in the 1–2  $\mu\text{m}$  range.

highlight the defined edges and “jigsaw-like” morphology of the  $\text{Bi}_2\text{WO}_6$  nanosheets formed by this route.

We obtained similar results for the reaction over a range of temperatures (180–220 °C) and times (5–24 h). Nanosheet products can be isolated simply by filtering, grinding, and re-dispersing in isopropyl alcohol. Cesium ions remain in the filtrate, separate from the nanosheets, as shown by electrospray ionization mass spectrometry (Fig. S15†). In contrast to bulk  $\text{Bi}_2\text{WO}_6$ , which is yellowish in color,  $\text{Bi}_2\text{WO}_6$  nanosheet powders are white and disperse readily in water to yield pearlescent dispersions (Fig. S9†). Individual  $\text{Bi}_2\text{WO}_6$  nanosheets have lateral dimensions in the 1–2  $\mu\text{m}$  range, as measured by SEM (Fig. 3) and AFM (Fig. S10†), which are significantly larger than those prepared without a  $\text{Cs}_4\text{W}_{11}\text{O}_{36}^{2-}$  template.<sup>4</sup> The thickness range of typical  $\text{Bi}_2\text{WO}_6$  nanosheets is 5–15 nm according to electron microscopy images (Fig. S11 and S12†) and AFM measurements (Fig. S10†).

The Raman spectrum of these  $\text{Bi}_2\text{WO}_6$  nanosheets (Fig. S19†) is consistent with data in the literature.<sup>37</sup> Raman peaks at 828, 792, 708, 415, 301, 279, 257, and 220  $\text{cm}^{-1}$  correspond to the bending and stretching modes of  $\text{WO}_6$ , whereas those at 368 and 327  $\text{cm}^{-1}$  correspond to the bending modes of  $(\text{Bi}_2\text{O}_2)^{2+}$ . Other nano-morphologies, particularly flowerlike  $\text{Bi}_2\text{WO}_6$ , display similar peaks in the Raman spectra. In comparison to the Raman spectrum of a single crystal of  $\text{Bi}_2\text{WO}_6$ ,<sup>7</sup> we observe peak broadening for the  $\text{Bi}_2\text{WO}_6$  nanosheets, indicative of heterogeneous bond distances that may originate from strain and defects at the nanoscale.<sup>38</sup> The Raman spectrum of  $\text{Bi}_2\text{WO}_6$  nanosheets also exhibited some decreased peak intensities compared to single crystal  $\text{Bi}_2\text{WO}_6$ , primarily at 301, 279, 257 and 220  $\text{cm}^{-1}$ . Previous work by Mączka, *et al.* showed that decreased peak intensity can be correlated to a reduction in the  $\text{Bi}_2\text{WO}_6$  thickness.<sup>37</sup> The thin structure of  $\text{Bi}_2\text{WO}_6$  nanosheets presented here contributes to a decrease in the orthorhombic distortion, causing a decrease in band intensity.

### Optical properties of $\text{Bi}_2\text{WO}_6$ nanosheets

The molar extinction coefficient  $\epsilon$  of a colloidal dispersion of  $\text{Bi}_2\text{WO}_6$  nanosheets, approximately 280  $\text{m}^2 \text{mol}^{-1}$ , was determined from the slope of an absorbance at 281 nm *versus* concentration plot (Fig. S16†). This value is consistent with medium-intensity absorption, and the linear Beer–Lambert

relationship indicates that the nanosheets are uniformly dispersed and well-behaved in isopropyl alcohol.

Fig. 4 shows UV-vis diffuse reflectance data for  $\text{Bi}_2\text{WO}_6$  nanosheets and for comparison, flowerlike  $\text{Bi}_2\text{WO}_6$  previously described in the literature.<sup>8</sup> Both samples exhibit strong absorption bands below 350 nm, with an onset in the visible region at  $\sim 425$  nm. This onset wavelength is typical for nanostructured  $\text{Bi}_2\text{WO}_6$  and slightly blue shifted with respect to bulk  $\text{Bi}_2\text{WO}_6$ , which is consistent with the white color of  $\text{Bi}_2\text{WO}_6$  nanosheets.

The optical bandgaps of  $\text{Bi}_2\text{WO}_6$  nanosheets and flowerlike structures were estimated by the Tauc method for an indirect allowed electronic transition; the curves shown in Fig. 4 (inset) exhibit linear Tauc regions just beyond the absorption edges, and the intercepts of these lines with the photon energy axis provide bandgap values (Fig. S22†). The corresponding bandgap energies of these samples are the same within error,  $\sim 3.1$  eV. This value approaches the upper end of experimentally determined bandgaps for  $\text{Bi}_2\text{WO}_6$ . Comparable examples include  $\text{Bi}_2\text{WO}_6$  multilayered discs ( $\sim 2.9$  eV)<sup>17</sup> and hierarchical  $\text{Bi}_2\text{WO}_6$  microspheres (2.95–3.04 eV).<sup>36</sup> We note, however, that even literature values for bulk  $\text{Bi}_2\text{WO}_6$  vary widely (2.6–3.3 eV),<sup>39–42</sup> as does the use of direct vs. indirect bandgap semiconductor models. Although size, shape, and structure are known to strongly influence the electronic character of a material, it is challenging to rationalize any trend in previously reported  $\text{Bi}_2\text{WO}_6$  bandgap values.

### Photochromism of $\text{Bi}_2\text{WO}_6$

Upon UV irradiation, colloidal dispersions of these  $\text{Bi}_2\text{WO}_6$  nanosheets dramatically change appearance from milky white to black in color (Fig. 5 inset). Although there is only a slight change to gray after 15 min of UV irradiation, the color becomes saturated after  $\sim 30$  min. To further analyze this phenomenon,

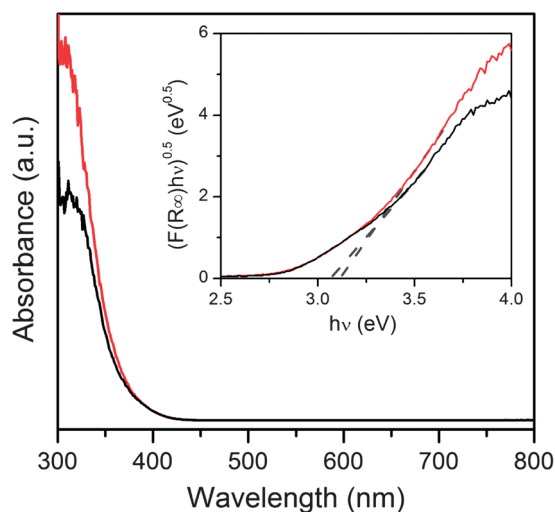


Fig. 4 UV-vis diffuse reflectance data for  $\text{Bi}_2\text{WO}_6$  nanosheets (black curve) and  $\text{Bi}_2\text{WO}_6$  flowerlike structures (red curve). Inset: corresponding Tauc plot used to estimate the optical bandgaps of these samples.

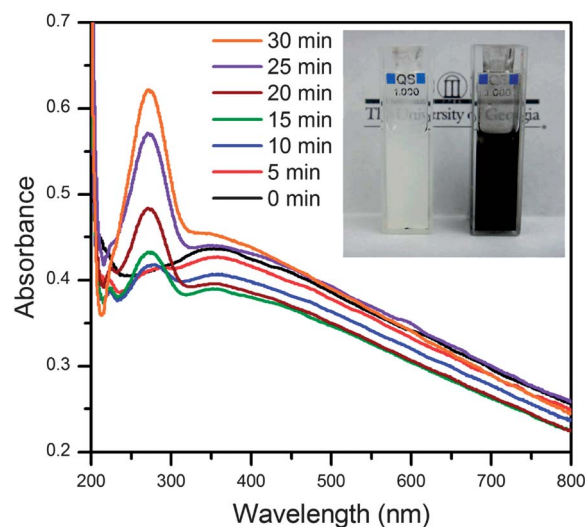


Fig. 5 UV-vis spectra of a UV-irradiated,  $1.3 \times 10^{-4}$  M dispersion of  $\text{Bi}_2\text{WO}_6$  nanosheets in isopropyl alcohol taken at 5 min intervals. Inset: photograph showing the dramatic color change of a concentrated  $\text{Bi}_2\text{WO}_6$  nanosheet dispersion before (white) and after (black) UV irradiation.

we tracked the absorbance of  $\text{Bi}_2\text{WO}_6$  nanosheets during UV irradiation. As shown in Fig. 5, UV-vis spectra were collected at 5 min intervals. The broad absorbance present at 230–600 nm in the starting material became less pronounced after 10 min as two new, strong peaks emerged at  $\lambda_{\text{max}}$  of  $\sim 273$  and  $\sim 203$  nm. After 30 min, this peak reached maximum intensity at  $\sim 0.2$  absorption units greater than the un-irradiated starting point. Fig. S17† provides a measure of the total change in absorbance over the course of this process.

Darkened  $\text{Bi}_2\text{WO}_6$  nanosheets could be isolated by centrifugation, and their color bleached completely upon either heating at  $105$  °C for 15 min or washing with copious amounts of water. UV-irradiated  $\text{Bi}_2\text{WO}_6$  nanosheets stored in the dark settle out of solution and turn gray in color, but the sample becomes black again after additional UV irradiation. The photochromism in this system showed good reversibility; cycling between colored and bleached states could be repeated three or more times.

To further elucidate the mechanism of color change,  $\text{Bi}_2\text{WO}_6$  nanosheets were evaluated in a variety of solvents. The resulting observations about the presence or absence of photochromic behavior (Table S1†) revealed that the photochromism of  $\text{Bi}_2\text{WO}_6$  nanosheets is highly solvent dependent. The color change occurred in alcohols, ethers, and amines yet not in water, amides, alkanes, or conjugated molecules (e.g., pyridine, benzyl alcohol). Many of the solvent environments that support photochromic behavior in this system are known to be “hole scavengers”, molecules that donate electrons to valence band holes created upon excitation. In  $\text{WO}_3$  and  $\text{TiO}_2$  nanoparticles, for example, such hole scavengers can suppress electron–hole recombination and thus allow trapped surface electrons to impact the visible absorption.<sup>25,43</sup> Likewise, conjugated molecules like benzyl alcohol are known as “electron scavengers” that promote electron–hole recombination.

For comparison, we evaluated the photochromic properties of flowerlike  $\text{Bi}_2\text{WO}_6$ ,<sup>8</sup> which exhibited a similar color change as the  $\text{Bi}_2\text{WO}_6$  nanosheets prepared in this work: from white to gray/black. However, the corresponding UV-vis spectra (Fig. S18†) showed a less dramatic change in absorption properties after UV irradiation.

Moreover, we observed that bulk  $\text{Bi}_2\text{WO}_6$  in single crystal form is photochromic as well; to our knowledge this property has not been reported previously for  $\text{Bi}_2\text{WO}_6$ —despite the fact that photochromism is well-known for many other tungsten oxide-based materials.<sup>25</sup> The pale yellow single crystals of  $\text{Bi}_2\text{WO}_6$  shown in the middle of Fig. 6 become distinctly gray in color (leftmost crystals) upon UV irradiation within a solvent-filled environment, and they maintain this color for days under ambient benchtop conditions. Dry solid samples did not exhibit photochromic behavior, however, which confirms the important role of the solvent in the mechanism.

$\text{Cs}_4\text{W}_{11}\text{O}_{36}^{2-}$  nanosheets, such as those used as the precursor/template for  $\text{Bi}_2\text{WO}_6$  nanosheets in this work, also are photochromic. Similar to the TBA- $\text{Cs}_4\text{W}_{11}\text{O}_{36}^{2-}$  nanosheets studied by Sasaki and co-workers,<sup>26</sup> a dispersion of  $\text{Cs}_4\text{W}_{11}\text{O}_{36}^{2-}$  nanosheets changes from colorless to blue upon UV irradiation. The corresponding UV-vis spectrum (Fig. S3†) shows a broad absorption at 600–1000  $\text{cm}^{-1}$  that is responsible for the blue color, but the overall change in absorption is less dramatic than that observed for  $\text{Bi}_2\text{WO}_6$  nanosheets.

Although the exact mechanism of photochromism in  $\text{Bi}_2\text{WO}_6$  is not yet known at this early point of study, we can make several informed observations.  $\text{Bi}_2\text{WO}_6$  clearly is different from both  $\text{WO}_3$  and  $\text{TiO}_2$  nanoparticles, two well-studied, inorganic photochromic systems. In the former case, the color change is believed to derive from photogenerated oxygen radicals trapped at defect sites, accompanied by metal reduction.<sup>25</sup> This situation is favored by high levels of oxygen vacancies, especially in amorphous  $\text{WO}_3$  samples. In the latter case, the color originates from stabilized surface electrons that lead to red-near infrared absorption.<sup>44</sup> Such surface electrons are highly sensitive to environmental conditions, *e.g.* solvent effects. In contrast to these cases, irradiated  $\text{Bi}_2\text{WO}_6$  absorbs strongly in the UV region rather than the red-infrared. Because the color change is robust, even upon isolation, it seems likely

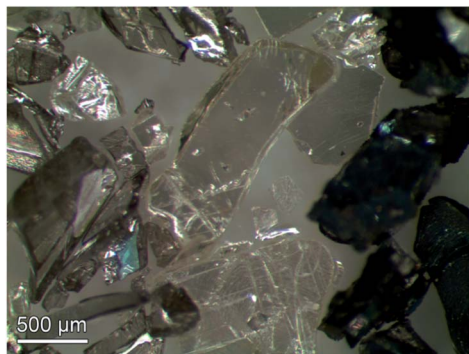


Fig. 6 Optical microscopy image of  $\text{Bi}_2\text{WO}_6$  (pale yellow crystals in center), UV-irradiated  $\text{Bi}_2\text{WO}_6$  (gray crystals at left), and Li-intercalated  $\text{Bi}_2\text{WO}_6$  (black crystals at right).

that the color centers correspond to reduced metal (bismuth and/or tungsten). Upon heating in air, these ions become re-oxidized and the material reverts back to its original color. In related work, Nozik and co-workers showed that excess donated electrons from hole scavengers could reduce  $\text{WO}_3$  to form  $\text{WO}_{3-x}$ .<sup>45</sup> The oxygen atoms in the  $(\text{Bi}_2\text{O}_2)^{2+}$  layers are weakly bound as well, and so oxygen dissociation may also occur here during surface reduction. Similar chemistry has been reported for  $\text{SrBi}_2\text{Ta}_2\text{O}_9$ , which contains the same layered  $\text{Bi}_2\text{O}_2$  motif.<sup>46</sup>

### Chromism of lithiated $\text{Bi}_2\text{WO}_6$

A related class of materials relevant to electrochromic devices is the tungsten bronzes, which like  $\text{Bi}_2\text{WO}_6$ , contain  $\text{WO}_6$  octahedra and structural vacancies accessible for intercalation.<sup>47,48</sup> The  $\text{WO}_3$  structure was found to greatly affect both the thermodynamics and kinetics of lithium intercalation into the material.<sup>49</sup>

Cruz and co-workers showed that lithium can be incorporated electrochemically into  $\text{Bi}_2\text{WO}_6$ ,<sup>50</sup> and Xie and co-workers investigated flowerlike  $\text{Bi}_2\text{WO}_6$  as an active electrode material in lithium-ion batteries.<sup>51</sup> Other reports have shown that lithium can be chemically incorporated into another Aurivillius-type layered perovskite oxide,  $\text{Bi}_4\text{Ti}_3\text{O}_{12}$ , using *n*-butyl lithium.<sup>52</sup> Upon intercalation, these crystals change from yellowish to black. This color change was attributed to the partial reduction of bismuth and titanium. Upon reacting with water, the lithiated samples broke into nanosized particles that the authors characterize as nanoplatelets. The exfoliation of layered transition metal dichalcogenides by this approach also can be quite successful; the reaction of  $\text{Li}^+$  within the van der Waals gap with water to generate  $\text{LiOH}$  and  $\text{H}_2$  forces the layers apart.<sup>53,54</sup>

We observed chromism upon the incorporation of lithium ions into  $\text{Bi}_2\text{WO}_6$  single crystals. The pale yellow crystals (Fig. 6 middle) turned brown-black in the presence of *n*-butyl lithium (Fig. 6 right), with a metallic appearance similar to tungsten bronze products (Fig. S20†).<sup>55</sup> The PXRD pattern of the lithiated  $\text{Bi}_2\text{WO}_6$  single crystals shows no change compared to bulk  $\text{Bi}_2\text{WO}_6$  before lithiation. Similar results have been reported for the lithiation of  $\text{Bi}_{3.25}\text{La}_{0.75}\text{Ti}_3\text{O}_{12}$ , another Aurivillius-phase material, with *n*-butyl lithium. In this study, Chevallier and co-workers determined that the intercalated lithium ions reside in the  $(\text{Bi}_2\text{O}_2)^{2+}$  layers and barely perturb the crystal structure.<sup>56</sup>

We hypothesize that the dramatic color change from pale yellow to brown-black arises from partial reduction of bismuth and tungsten, similar to the example of lithiated  $\text{Bi}_4\text{Ti}_3\text{O}_{12}$ .<sup>52</sup> A reversible color change also was observed in the  $\text{Bi}_{3.25}\text{La}_{0.75}\text{Ti}_3\text{O}_{12}$  system.<sup>56</sup>

As in prior studies, we removed lithium from lithiated  $\text{Bi}_2\text{WO}_6$  by water treatment under mild sonication. The crystals returned to a pale yellow color, although they also clearly became smaller, as indicated by PXRD peak broadening (Fig. 7 top trace). When mm-sized  $\text{Bi}_2\text{WO}_6$  crystals were used in this reaction sequence, we obtained the mixture shown in Fig. 8A: a white aqueous dispersion of irregular  $\text{Bi}_2\text{WO}_6$  nanoparticles, characterized by TEM (Fig. 8B and C), and small yellow crystals of  $\text{Bi}_2\text{WO}_6$  at the bottom of the vial. These results are

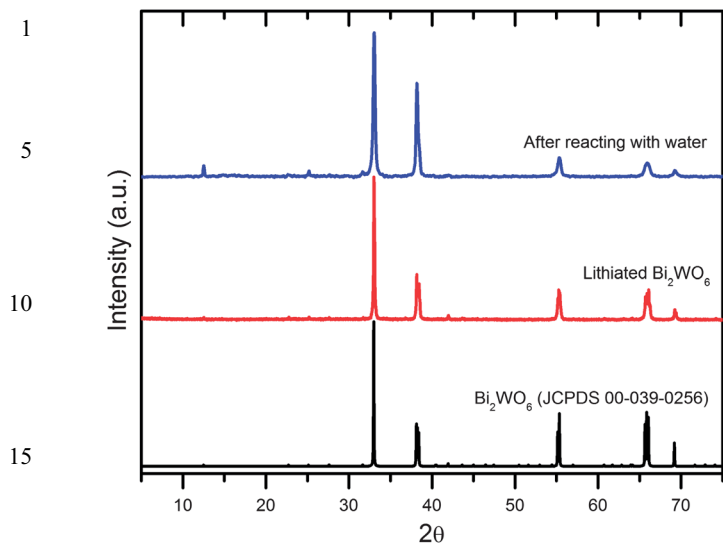


Fig. 7 PXRD patterns of  $\text{Bi}_2\text{WO}_6$  reference (black), ground lithiated single crystals (red) and after reacting with water (blue).

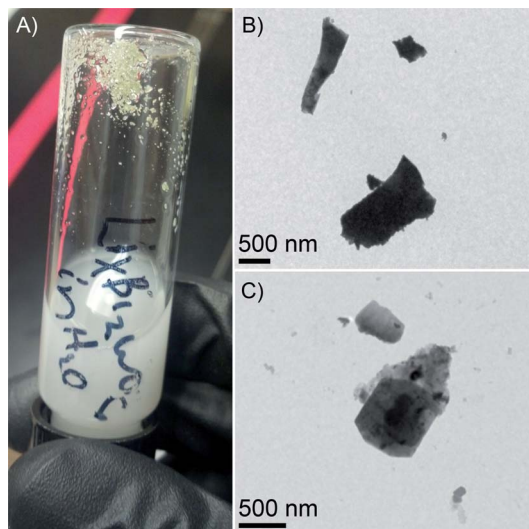


Fig. 8 (A) Inverted vial of dispersed  $\text{Bi}_2\text{WO}_6$  and remaining  $\text{Bi}_2\text{WO}_6$  crystals prepared by reacting lithiated  $\text{Bi}_2\text{WO}_6$  with water. (B and C) TEM images of  $\text{Bi}_2\text{WO}_6$  nano-particulates located in the white dispersion.

consistent with lithiation of only the outermost portion of the large  $\text{Bi}_2\text{WO}_6$  crystals, followed by fragmentation that leaves the unreacted inner core behind. In contrast, powdered  $\text{Bi}_2\text{WO}_6$  (ground single crystals) was completely degraded by these lithiation conditions, resulting in an amorphous PXRD pattern.

## Conclusions

In this contribution, we have described a successful approach to making highly anisotropic nanosheets of  $\text{Bi}_2\text{WO}_6$  with large lateral dimensions (1–2  $\mu\text{m}$ ) and 5–15 nm thicknesses. Lateral

control can be achieved through the use of a  $\text{Cs}_4\text{W}_{11}\text{O}_{36}^{2-}$  nanosheet template. In this reaction, the initial bismuth source,  $\text{Bi}(\text{NO}_3)_3$ , transforms into  $[\text{Bi}_6\text{O}_5(\text{OH})_3](\text{NO}_3)_5 \cdot 3\text{H}_2\text{O}$  within 0.5 h, and after 1 h becomes  $[\text{Bi}_6\text{O}_6(\text{OH})_3](\text{NO}_3)_3 \cdot 1.5\text{H}_2\text{O}$ , which was found to be the bismuth source relevant to the formation of  $\text{Bi}_2\text{WO}_6$  nanosheets. The layered  $\text{Bi}_2\text{WO}_6$  nanosheets are formed after 5 h at solvothermal conditions. Without the  $\text{Cs}_4\text{W}_{11}\text{O}_{36}^{2-}$  nanosheet template, flowerlike cluster are formed instead.

Optical characterization of  $\text{Bi}_2\text{WO}_6$  nanosheets shows that they absorb strongly in the UV and have a relatively high band gap of  $\sim 3.1$  eV. The most surprising result is the photochromic behavior of  $\text{Bi}_2\text{WO}_6$  in nanosheet, flowerlike, and single crystal forms. Although not yet examined in detail, we propose that the mechanism of white to black color change in this system involves bismuth and/or tungsten reduction. Notably, the color change is robust and reversible.

Additionally, lithium ions can be intercalated chemically into the  $\text{Bi}_2\text{WO}_6$  structure through the use of *n*-butyl lithium. This reaction provides another example of  $\text{Bi}_2\text{WO}_6$  chromism, in this case pale yellow to brown-black. The subsequent reaction of lithiated  $\text{Bi}_2\text{WO}_6$  with water provides nanofragments of  $\text{Bi}_2\text{WO}_6$  rather than nanosheets. We conclude that our  $\text{Cs}_4\text{W}_{11}\text{O}_{36}^{2-}$  nanosheet templating approach remains the most effective way to prepare and isolate large  $\text{Bi}_2\text{WO}_6$  nanosheets.

## Experimental

### Preparation of $\text{Bi}_2\text{WO}_6$ nanosheets

0.6956 g (1.43 mmol) of  $\text{Bi}(\text{NO}_3)_3 \cdot 5\text{H}_2\text{O}$  and 4.2 mL of a 15.5 mM aqueous solution of  $\text{Cs}_4\text{W}_{11}\text{O}_{36}^{2-}$  nanosheets (7.90 mmol) were mixed thoroughly in an agate mortar. Once homogeneous, this mixture was diluted to  $\sim 30$  mL total and stirred at room temperature for 2–4 h. Then this dispersion was transferred to a 42 mL Teflon-lined autoclave and heated at  $220^\circ\text{C}$  for 6 h. The resulting  $\text{Bi}_2\text{WO}_6$  nanosheets were collected by vacuum filtration using a  $0.4 \mu\text{m}$  membrane filter, and they were washed with deionized water followed by ethanol. Isolated yield of dried  $\text{Bi}_2\text{WO}_6$  nanosheet powder was 0.4852 g (97% yield). For characterization and subsequent experiments, this powder was hand ground with a mortar/pestle and then dispersed in water with mild bath sonication. For the time study, a homogenous mixture of the precursors was divided into individual autoclaves and heated at  $180^\circ\text{C}$  for the reported times. The products were collected by vacuum filtration and then re-dispersed for analysis.

### UV irradiation experiments

Typical UV irradiation experiments were performed on samples of  $\sim 35$  mg  $\text{Bi}_2\text{WO}_6$  dispersed in 5 mL solvent, unless another concentration is specified. Dispersions were placed in  $1 \text{ cm}^2$  double-sided cuvettes and irradiated for 2 h with a quartz mercury vapor grid lamp with a power of  $450 \mu\text{W cm}^{-2}$ , located 5 cm away from the sample.

## Intercalation of Bi<sub>2</sub>WO<sub>6</sub> with lithium

A typical method for the intercalation of lithium into Bi<sub>2</sub>WO<sub>6</sub> entails the following: within an Ar-filled glovebox, place 0.25 g of bulk Bi<sub>2</sub>WO<sub>6</sub> (0.35 mmol) into 2 mL of dry hexane and carefully add 1.4 mL of 2.5 M *n*-butyl lithium (3.5 mmol). Seal and stir at room temperature for 3–5 days. The lithiated product was filtered under an argon atmosphere *via* gravity filtration, rinsed with excess hexane, and stored under argon prior to optical microscopy and PXRD analysis. Subsequent reaction of lithiated bismuth tungstate in water is accomplished by bath sonication for 1–2 h.

## Characterization details

PXRD patterns were collected using a Bruker D8-Advance diffractometer (Co-K $\alpha$  radiation source) operated at 40 mA and 40 kV. All samples were collected from 3–75 2 $\theta$  with a rate of 0.1 seconds per step. Samples were prepared by pressing the dry powders into an aluminum mount.

Electron microscopy samples were prepared with samples dispersed in isopropanol using bath sonication. TEM images were attained using a FEI Tecnai 20 (200 keV) microscope. SEM samples were drop cast onto gold-coated silicon wafers, and images were collected with a FEI Inspect F field emission gun scanning electron microscope operated at 10 keV.

UV-vis absorption spectra were collected using a Cary 50 UV-visible spectrometer, with a scanning range of 200 to 1100 nm. UV-vis diffuse reflectance spectra were collected with a Shimadzu 2450 UV-vis spectrophotometer outfitted with an integration-sphere detector. Diffuse reflectance samples consisted of powders packed into a 1 × 2 × 4 mm sample holder.

## Acknowledgements

This work was supported by a U.S. Department of Energy Office of Science Early Career Research Program Award (Office of Basic Energy Sciences, DE-SC0008065). We thank Prof. Zhengwei Pan (UGA) for use of the UV-vis spectrophotometer in his laboratory.

## Notes and references

- 1 B. Aurivillius, *Ark. Kemi*, 1952, **5**, 39–47.
- 2 Y. Noguchi and M. Miyayama, in *Lead-Free Piezoelectrics*, ed. S. Priya and S. Nahm, Springer, New York, 2012, pp. 405–459.
- 3 Y. Yoneda, S. Kohara, H. Takeda and T. Tsurumi, *Jpn. J. Appl. Phys.*, 2012, **51**, 09LE06.
- 4 C. Zhang and Y. Zhu, *Chem. Mater.*, 2005, **17**, 3537–3545.
- 5 L. Zhang, H. Wang, Z. Chen, P. K. Wong and J. Liu, *Appl. Catal., B*, 2011, **106**, 1–13.
- 6 J. Tang, Z. Zou and J. Ye, *Catal. Lett.*, 2004, **92**, 53–56.
- 7 H. Takeda, J. S. Han, M. Nishida, T. Shiosaki, T. Hoshina and T. Tsurumi, *Solid State Commun.*, 2010, **150**, 836–839.
- 8 L. Zhang, W. Wang, Z. Chen, L. Zhou, H. Xu and W. Zhu, *J. Mater. Chem.*, 2007, **17**, 2526–2532.
- 9 J. Xia, H. Li, Z. Luo, H. Xu, K. Wang, S. Yin and Y. Yan, *Mater. Chem. Phys.*, 2010, **121**, 6–9.

- 10 H. Fu, L. Zhang, W. Yao and Y. Zhu, *Appl. Catal., B*, 2006, **66**, 100–110.
- 11 Y. Li, J. Liu, X. Huang and G. Li, *Cryst. Growth Des.*, 2007, **7**, 1350–1355.
- 12 L. Zhang, W. Wang, L. Zhou and H. Xu, *Small*, 2007, **3**, 1618–1625.
- 13 M. Shang, W. Wang, S. Sun, L. Zhou and L. Zhang, *J. Phys. Chem. C*, 2008, **112**, 10407–10411.
- 14 L. Wu, J. Bi, Z. Li, X. Wang and X. Fu, *Catal. Today*, 2008, **131**, 15–20.
- 15 D. Ma, S. Huang, W. Chen, S. Hu, F. Shi and K. Fan, *J. Phys. Chem. C*, 2009, **113**, 4369–4374.
- 16 C. Xu, X. Wei, Z. Ren, Y. Wang, G. Xu, G. Shen and G. Han, *Mater. Lett.*, 2009, **63**, 2194–2197.
- 17 C. Xu, X. Wei, Y. Guo, H. Wu, Z. Ren, G. Xu, G. Shen and G. Han, *Mater. Res. Bull.*, 2009, **44**, 1635–1641.
- 18 Y. Zhou, K. Vuille, A. Heel and G. R. Patzke, *Z. Anorg. Allg. Chem.*, 2009, **635**, 1848–1855.
- 19 C. Wang, H. Zhang, F. Li and L. Zhu, *Environ. Sci. Technol.*, 2010, **44**, 6843–6848.
- 20 Y. Tian, G. Hua, W. Xu, N. Li, M. Fang and L. Zhang, *J. Alloys Compd.*, 2011, **509**, 724–730.
- 21 J.-C. Champarnaud-Mesjard, B. Frit and A. Watanabe, *J. Mater. Chem.*, 1999, **9**, 1319–1322.
- 22 R. E. Schaak and T. E. Mallouk, *Chem. Commun.*, 2002, 706–707.
- 23 M. R. Waller, T. K. Townsend, J. Zhao, E. M. Sabio, R. L. Chamousis, N. D. Browning and F. E. Osterloh, *Chem. Mater.*, 2012, **24**, 698–704.
- 24 Y. Shigesato, *Jpn. J. Appl. Phys., Part 1*, 1991, **30**, 1457–1462.
- 25 T. He and J. Yao, *J. Mater. Chem.*, 2007, **17**, 4547–4557.
- 26 K. Fukuda, K. Akatsuka, Y. Ebina, R. Ma, K. Takada, I. Nakai and T. Sasaki, *ACS Nano*, 2008, **2**, 1689–1695.
- 27 C. G. Granqvist, *Solid State Ionics*, 1992, **53–56**(1), 479–489.
- 28 A. Karuppasamy and A. Subrahmanyam, *Thin Solid Films*, 2007, **516**, 175–178.
- 29 G. A. Niklasson and C. G. Granqvist, *J. Mater. Chem.*, 2007, **17**, 127–156.
- 30 K. Bange and T. Gambke, *Adv. Mater.*, 1990, **2**, 10–16.
- 31 K. Fukuda, K. Akatsuka, Y. Ebina, M. Osada, W. Sugimoto, M. Kimura and T. Sasaki, *Inorg. Chem.*, 2012, **51**, 1540–1543.
- 32 K. Okada, F. Marumo and S. Iwai, *Acta Crystallogr., Sect. B: Struct. Crystallogr. Cryst. Chem.*, 1978, **34**, 50–54.
- 33 N. Henry, M. Evain, P. Deniard, S. Jovic, F. Abraham and O. Mentre, *Z. Naturforsch., B: Chem. Sci.*, 2005, **60**, 322–327.
- 34 K. S. Knight, *Mineral. Mag.*, 1992, **56**, 399–409.
- 35 L. Xie, J. Wang, Y. Hu, Z. Zheng, S. Weng, P. Liu, X. Shi and D. Wang, *Mater. Chem. Phys.*, 2012, **136**, 309–312.
- 36 Y. Zhou, E. Antonova, W. Bensch and G. R. Patzke, *Nanoscale*, 2010, **2**, 2412–2417.
- 37 M. Mączka, L. Macalik, K. Hermanowicz, L. Kepinski and P. Tomaszewski, *J. Raman Spectrosc.*, 2010, **41**, 1059–1066.
- 38 A. K. P. Mann, E. M. P. Steinmiller and S. E. Skrabalak, *Dalton Trans.*, 2012, **41**, 7939–7945.
- 39 S. Mahanty and J. Ghose, *Mater. Lett.*, 1991, **11**, 254–256.
- 40 Y. Huang, Z. Ai, W. Ho, M. Chen and S. Lee, *J. Phys. Chem. C*, 2010, **114**, 6342–6349.

- 1 41 L. Zhou, M. Yu, J. Yang, Y. Wang and C. Yu, *J. Phys. Chem. C*, 2010, **114**, 18812–18818.
- 42 C. Bhattacharya, H. C. Lee and A. J. Bard, *J. Phys. Chem. C*, 2013, **117**, 9633–9640.
- 5 43 M. Jakob, H. Levanon and P. V. Kamat, *Nano Lett.*, 2003, **3**, 353–358.
- 44 I. Bedja, S. Hotchandani and P. V. Kamat, *J. Phys. Chem.*, 1993, **97**, 11064–11070.
- 10 45 M. T. Nenadovic, T. Rajh, O. I. Micic and A. J. Nozik, *J. Phys. Chem.*, 1984, **88**, 5827–5830.
- 46 Y. Shimakawa and Y. Kubo, in *MRS Proceedings*, Cambridge Univ Press, 2000.
- 47 J. D. Guo and M. S. Whittingham, *Int. J. Mod. Phys. B*, 1993, **7**, 4145–4164.
- 15 48 N. Kumagai, A. Yu and H. Yashiro, *Solid State Ionics*, 1997, **98**, 159–166.
- 49 C. O. Avellaneda, *Mater. Sci. Eng., B*, 2007, **138**, 123–127.
- 50 F. E. Longoria Rodríguez and A. Martínez-de la Cruz, *Mater. Res. Bull.*, 2001, **36**, 1195–1204.
- 51 J. Wu, F. Duan, Y. Zheng and Y. Xie, *J. Phys. Chem. C*, 2007, **111**, 12866–12871.
- 52 J.-Y. Kim, I. Chung, J.-H. Choy and G.-S. Park, *Chem. Mater.*, 2001, **13**, 2759–2761.
- 53 D. W. Murphy, F. J. Di Salvo, G. W. Hull and J. V. Waszczak, *Inorg. Chem.*, 1976, **15**, 17–21.
- 10 54 P. Joensen, R. F. Frindt and S. R. Morrison, *Mater. Res. Bull.*, 1986, **21**, 457–461.
- 55 K. Bange, *Sol. Energy Mater. Sol. Cells*, 1999, **58**, 1–131.
- 15 56 V. Chevallier, G. Nihoul and V. Madigou, *J. Solid State Chem.*, 2008, **181**, 439–449.
- 20
- 25
- 30
- 35
- 40
- 45
- 50
- 55